The International Journal of Advanced Manufacturing Technology (2020) 109:2481–2490
https://doi.org/10.1007/s00170-020-05821-w

ORIGINAL ARTICLE

Analytical modeling of the heat-affected zone in laser-assisted milling of AerMet100 steel

Haohao Zeng[1] · Rong Yan[1] · Wei Wang[1] · Hang Zhang[1] · Jingnan Yan[1] · Fangyu Peng[2]

Received: 9 December 2019 / Accepted: 23 July 2020 / Published online: 1 August 2020

Abstract
Compared with conventional milling, laser-assisted milling (LAM) enhances the productivity of difficult-to-cut materials and is a green process due to the elimination of coolant. However, this heat-assisted process may induce a detrimental heat-affected zone (HAZ, generally referred to as phase transformation zone) in the workpiece. This paper presents an analytical model to predict the HAZ produced by laser heating in LAM of AerMet100 steel, in which the size of HAZ is determined by comparing the steady temperature field with the phase transformation temperature of workpiece material. A series of laser heating and LAM experiments are performed to validate the HAZ model. XRD technique is employed to analyze the microstructures in the heated and machined surface layers. Phase compositions and retained austenite content of each specimen are compared with those of the base material. The results indicate that the proposed model is feasible. In addition, the effects of different laser parameters on the HAZ are discussed. The size of the HAZ increases significantly with increasing laser power and decreases significantly with increasing feed speed. The HAZ width increases with the increase of laser spot size, and it appears the opposite change for the HAZ depth. This work can be applied to determine the process parameters in LAM that will yield no residual HAZ in the workpiece after machining.

Keywords Heat-affected zone · Phase transformation · Laser heating · Laser-assisted milling · AerMet100 steel

1 Introduction

Ultrahigh strength steel (AerMet100) has been widely used to manufacture important structural parts which sustain high stress in aviation and aerospace industry, such as landing gear and rocket shell [1]. However, AerMet100 steel is difficult to machine due to its high strength, high toughness, and low thermal conductivity, and easy to be adhered on tool face [2]. Conventional machining of AerMet100 steel is a low productivity process with a high material running cost, such as consumption of cutting tools and coolant. LAM is a well-proved method to enhance the machinability of difficult-to-cut materials. Many researchers [3–7] have demonstrated that LAM leads to a smaller cutting force and longer tool life than conventional machining. However, it is a heat-assisted process and may induce a detrimental HAZ in the workpiece. In the HAZ, the microstructure is changed and can cause a change of the mechanical strength [8]. Therefore, the HAZ generated in laser-assisted machining has been widely concerned.

Tagliaferri et al. [9] characterized the laser heating process by detecting how the individual LAM parameters influence working temperature, HAZ extension, and laser track width. Pan et al. [10] characterized the melting zone shape in the LAM process of Inconel 718. The effects of laser scanning speed and power input on the melting zone shape were investigated. Singh et al. [11] analyzed the HAZ generated by laser heating of H-13 steel for changes in microstructure and microhardness. A finite element (FE) model was established to predict the temperature distribution in workpiece. The critical temperature corresponding to the HAZ depth was identified to be close to the austenization temperature. Yang et al. [12]

✉ Rong Yan
yanrong@hust.edu.cn

Haohao Zeng
mzh1825@126.com

[1] National NC System Engineering Research Center, School of Mechanical Science and Engineering, Huazhong University of Science and Technology, Wuhan 430074, China

[2] State Key Lab of Digital Manufacturing Equipment and Technology, School of Mechanical Science and Engineering, Huazhong University of Science and Technology, Wuhan 430074, China

developed a FE model to predict the HAZ produced by laser heating of Ti6Al4V alloy in LAM process. The beta transit temperature was taken as the critical value for the formation of HAZ. Parametric studies showed that the size of the HAZ increases with increasing of laser power and decreases with the increase of laser spot size and laser scanning speed. Rahim et al. [13] presented a FE model to predict the temperature distribution caused by laser heating. The numerical model was validated by comparing predicted and measured geometries of melting pool and HAZ.

A suitable combination of cutting parameters and laser parameters makes full use of the advantages of LAM, as well as ensuring that the HAZ is completely removed. Wiedenmann and Zaeh [5] established a process model which provided a basis for the determination of process parameters in LAM. Three thermal boundary conditions were proposed in the model for a reliable and economic machining operation. Similar boundary conditions were applied in other literatures [14, 15]. Recently, Shang et al. [16] proposed a novel spatially and temporally controlled laser heating method, in which a large area can be heated up with a small laser spot by controlling the beam scanning. The laser configuration for the prescribed HAZ was achieved by solving the inverse heat conduction problem where the laser power together with either laser path or laser speed was optimized.

The absorptivity of workpiece material has a significant effect on the temperature distribution in LAM. Kashani et al. [4] presented two methods for calculating this coefficient based on the surface temperature obtained from measurement by a pyrometer and an analytical model of the process. Yang et al. [12] developed an indirect method for calculating absorptivity by using analytical method and the measured maximum temperature on the top surface of workpiece. Kim and Lee [17] calibrated the absorptivity of Inconel 718 by conducting preheating experiments using a high-power diode laser. Singh et al. [11] determined the absorptivity by calibrating the thermal model against a measured temperature at a known workpiece location. This method has also been adopted by other researchers [14, 18].

A number of models were proposed to predict the temperature distribution and HAZ caused by laser heating in LAM process, but most of them were developed based on the commercial FE software. Compared with the FE method, the analytical method can not only achieve a fast prediction of HAZ but also allow one to understand the influence mechanism of each process parameter on HAZ.

The main purpose of this paper is to establish an accurate analytical model, which is capable of predicting the HAZ produced by laser heating in LAM process. In Section 2, the modeling procedure of HAZ is elaborated. The absorptivity of AerMet100 steel is calibrated in Section 3. Section 4 introduces model verification and discussion. Conclusions of the entire study are drawn in Section 5.

2 Prediction of HAZ

In order to ensure the machined surface quality, the HAZ caused by laser heating in LAM process should be completely removed. An analytical model is presented in this section to predict the HAZ during laser heating of AerMet100 steel.

2.1 Temperature field during laser heating

During laser heating process, a laser beam irradiates on the top surface of workpiece and moves at a constant speed, as shown in Fig. 1. Affected by the laser incident angle, the laser spot is elliptic in shape. By setting the laser spot center as the origin, the laser beam moving direction as the ***OX*** axis, the workpiece height direction as the ***OZ*** axis, the heat source coordinate system ***OXYZ*** is established. It should be noted that the heat source coordinate system moves with the laser beam at the same speed. In addition, the origin of the time axis is defined at the moment when one-half of the laser beam irradiates on the workpiece.

According to the test result of the laser beam, its power density approximately obeys Gaussian distribution. In order to analytically calculate the temperature field caused by laser heating, the plane heat source should be discretized into point heat sources, as shown in Fig. 2.

Taking an arbitrary point heat source Q_{ij} (shown in Fig. 2) as an example, its power density can be written as follow:

$$P_{ij} = \frac{2P_0}{\pi r_a r_b} \exp\left(-2x_{ij}^2/r_a^2 - 2y_{ij}^2/r_b^2\right) \quad (1)$$

where P_0 is the output power of the laser beam. r_a and r_b are the semi-major and semi-minor axes of the laser spot, respectively. x_{ij} and y_{ij} are the coordinates of Q_{ij} in the heat source coordinate system ***OXYZ***.

The temperature distribution in workpiece can be determined by using the analytical model of a moving point heat source acting over a semi-infinite medium [19, 20]. Take an arbitrary point ***M*** in workpiece as an example. At any given

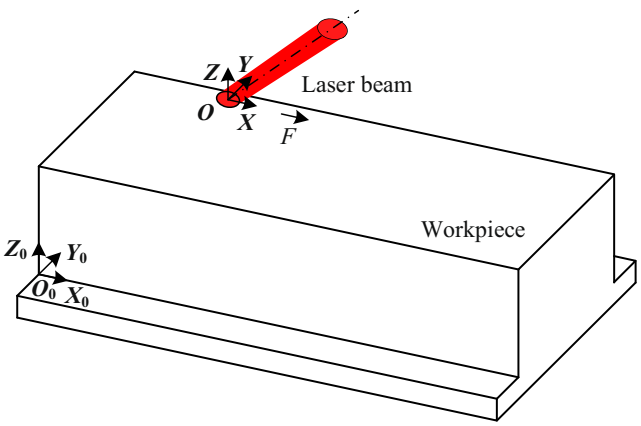

Fig. 1 Laser heating schematic figure

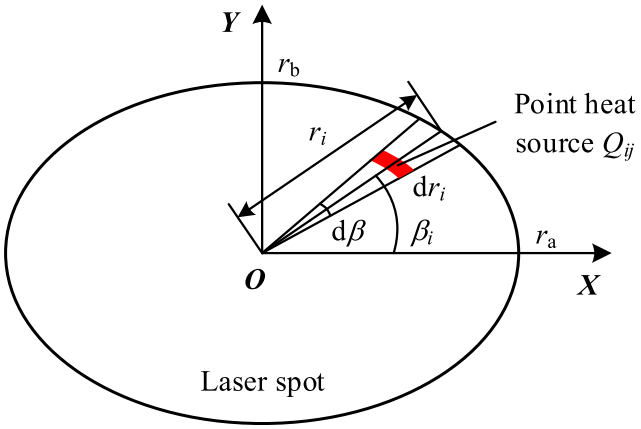

Fig. 2 The discretization of laser heat source

time t, the temperature rise at point $\boldsymbol{M}$ caused by the point heat source Q_{ij} can be calculated as follows:

$$d\theta_{1,ij}(x_0, y_0, z_0, t) = \frac{a_0 P_{ij} S_{ij}}{2\pi\lambda s} \exp\left(-F\frac{s + x_0 - x_{1ij}}{2a}\right) \quad (2)$$

where x_0, y_0, and z_0 are the coordinates of point $\boldsymbol{M}$ in the workpiece coordinate system $\boldsymbol{O_0X_0Y_0Z_0}$ (shown in Fig. 1). a_0 is the absorptivity of workpiece material. S_{ij} is the area of the point heat source Q_{ij}, which can be determined by Eq. (3). λ and α are the thermal conductivity and thermal diffusivity of workpiece material, respectively. s is the distance between the researched point $\boldsymbol{M}$ and the point heat source Q_{ij}. F is the feed speed of the laser beam. x_{1ij} is the x-coordinate of Q_{ij} in $\boldsymbol{O_0X_0Y_0Z_0}$. Considering the movement of laser beam, both s and x_{1ij} change with time t.

$$S_{ij} = \frac{1}{2}\left[(r_1 - j\mathrm{d}r_i + \mathrm{d}r_i)^2 - (r_i - j\mathrm{d}r_i)^2\right]\mathrm{d}\beta \quad (3)$$

where r_i is the polar diameter, which can be calculated by Eq. (4). dr_i and $d\beta$ are radial and angular discrete spacing, respectively. $d\beta = 2\pi/N_1$, $dr_i = r_i/N_2$, N_1 and N_2 are the angular and radial discrete numbers of the laser heat source respectively.

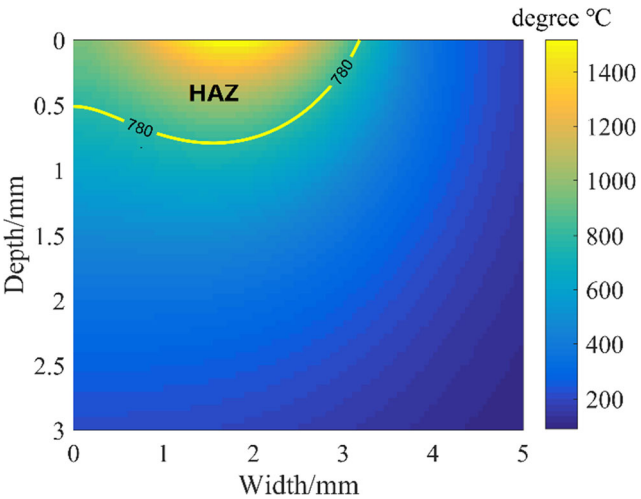

Fig. 3 The heat-affected zone of material

Table 1 Material properties of AerMet100 steel

Elastic modulus (GPa)	Yield strength (MPa)	Thermal conductivity (W/m °C)	Thermal diffusivity (m^2/s)	Hardness (HRC)
206	831.8	19.3	5.9×10^{-6}	42

$$r_i = r_a r_b / \sqrt{(r_a \sin\beta_i)^2 + (r_b \cos\beta_i)^2} \quad (4)$$

where β_i is the polar angle.

During side milling process, the laser spot moves along the workpiece boundary, as shown in Fig. 1. To tackle the boundary issue of heat conduction in workpiece, the image heat source method [21–23] is applied here. Therefore, the transient temperature at point $\boldsymbol{M}$ during laser heating process can be determined as follows:

$$T(x_0, y_0, z_0 t) = T_r + \sum_{i=1}^{N_1}\sum_{j=1}^{N_2}\left(d\theta_{1,ij} + d\theta_{1l,ij}\right) \quad (5)$$

where T_r is the ambient temperature. $d\theta_{1l,ij}$ is the temperature rise at point $\boldsymbol{M}$ caused by the image heat source of Q_{ij}.

Based on the methodology presented above, the temperature variation history of point $\boldsymbol{M}$ can be obtained by changing the given time t. If the simulation process is applied to a dot-matrix in workpiece, the temperature field can be determined.

2.2 HAZ model

AerMet100 steel is mainly composed of martensite. During laser heating process, any point in workpiece undergoes heating and cooling processes. If the peak temperature at the

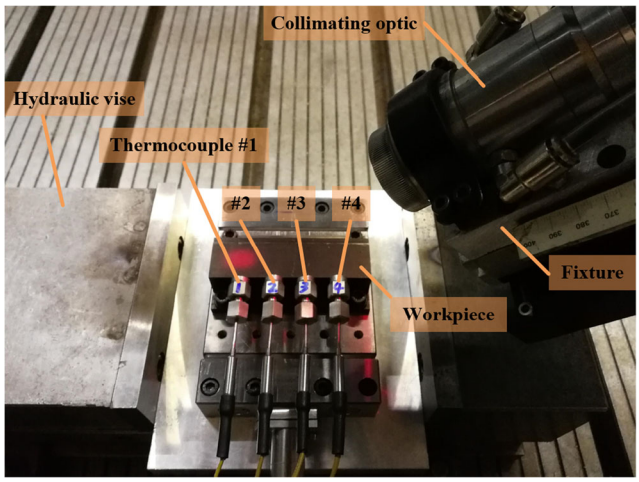

Fig. 4 Laser heating experimental image

Table 2 Laser heating experimental parameters (calibration experiments)

No.	Power (W)	Feed speed (mm/min)
1	200	50
2	200	100
3	250	50
4	250	100
5	500	50
6	500	100
7	1000	50
8	1000	100
9	1000	200

researched point exceeds the austenization temperature of AerMet100 steel, the original structure will transform into austenite.

In this paper, the area where the microstructure changes is defined as the HAZ. Based on the thermal model proposed in the above section, the size of the HAZ can be determined by comparing the steady temperature field with the phase transformation temperature of workpiece material.

Considering that the steady temperature field is independent of x-coordinate and time t, only the temperature distribution in the cross section (parallel to the plane $\boldsymbol{O_0Y_0Z_0}$) should be considered. In order to calculate the size of the HAZ, a function T_d is defined here:

$$T_d(y_0, z_0) = T(y_0, z_0) - T_0 \qquad 0 \le y_0 \le W; 0 \le z_0 \le H \tag{6}$$

where T_0 is the phase transformation temperature of workpiece material, which is about 780 °C (austenization temperature) for AerMet100 steel [24]. y_0 and z_0 are the coordinates of the researched point in $\boldsymbol{O_0X_0Y_0Z_0}$. W and H are the width and height of workpiece, respectively.

Based on the above analysis, it is not hard to find that the HAZ is the area where the function value is non-negative, as shown in Fig.3.

3 Calibration of absorptivity

Absorptivity is an important material parameter in laser-assisted machining, as it defines the ratio of the energy absorbed by workpiece material to the total laser energy input. In this section, a series of laser heating experiments were conducted to calibrate the absorptivity of AerMet100 steel, and an empirical formula of absorptivity was obtained by least squares fitting.

3.1 Experimental setup

The workpiece was a block of AerMet100 steel (after blackening treatment) with a length of 100 mm, a width of 30 mm, and a height of 30 mm. The main material properties of AerMet100 steel are listed in Table 1. A diode laser system (HDLS-1000) with a maximum power of 1000 W and a wavelength of 915 nm was used to generate a laser beam. The laser beam was transmitted along a 15-m-long optical fiber of 0.4-mm diameter terminated with a collimating optic. Then, the laser was focused on the top surface of workpiece with a focusing lens of 200-mm focal length. The collimating optic was mounted on a fixture, which in turn was mounted on the spindle. The fixture consisting of three moving pairs and one rotating pair was used to adjust laser incident angle (the angle between laser beam and spindle), spot size, and laser-tool distance (the distance between tool center and laser spot center) in LAM.

Nine laser heating experiments were carried out on a self-built LAM platform as shown in Fig. 4. The experimental scheme is shown in Table 2, where four laser powers and three feed speeds are involved. In addition, the laser beam was tilted 45° in the feed direction; the semi-minor axis of the laser spot was equal to 1.8 mm.

As displayed in Fig. 4, temperature signals were collected by INOR fast response thermocouples and recorded by a NI data acquisition system during laser heating processes. In each experiment, four K-type thermocouples with a diameter of

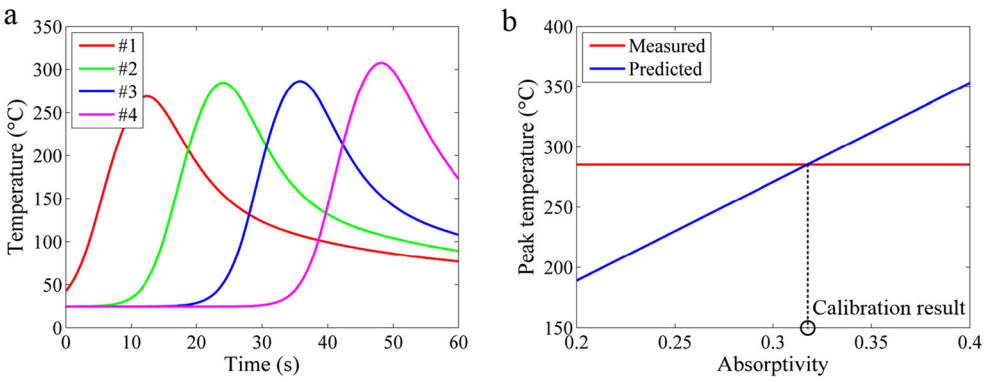

Fig. 5 Temperature variation histories of four researched points in workpiece: **a** measured results, **b** comparison of predicted and measured results

Table 3 Calibration results

No.	Average peak temperature (°C)	Calibrated absorptivity	Predicted peak temperature (°C)	Error (%)
1	172.0	0.350	168.3	2.2
2	138.8	0.347	143.4	3.3
3	204.2	0.342	198.1	3.0
4	167.5	0.347	168.0	0.3
5	331.3	0.292	336.3	1.5
6	285.3	0.317	282.1	1.1
7	574.7	0.262	584.7	1.7
8	484.4	0.280	487.3	0.6
9	364.2	0.304	357.3	1.9

2 mm were inserted into workpiece uniformly. Thermocouple #1 was 20 mm away from workpiece side and 20 mm away from #2. The insertion depth of each thermocouple was 25 mm. The horizontal and vertical distances between each thermocouple tip and the laser spot center were 3.2 mm and 2 mm, respectively.

3.2 Results and analysis

In order to illustrate the calibration procedure of absorptivity, experiment no. 6 was taken as an example here. The measured temperature curves are shown in Fig. 5a. The temperature at each measuring point increases first and then decreases during laser heating process. Peak temperature of the first measuring point is the lowest, and that of the last measuring point is the highest. Besides, peak temperatures of the middle two measuring points are very close. The above experimental phenomena are mainly caused by the heat conduction boundary, because the workpiece is not infinitely long.

Peak temperatures measured by thermocouples #2 and #3 in each experiment were averaged, and the result was used to calibrate the absorptivity. As can be seen in Fig. 5b, the predicted results of peak temperature under different absorptivity conditions were firstly compared with the measured result. Then, the absorptivity that makes the predicted value closest to the measured value can be taken as the calibration result.

The calibrated absorptivity of each experiment is listed in Table 3. Take experiment no. 6 as an example, the calibrated absorptivity is equal to 0.317. When the laser power increases from 200 to 1000 W, the absorptivity has a sharp decrease. This experimental phenomenon is similar to that reported in [8]. Besides, the absorptivity increases slightly with the increase of feed speed.

In order to consider the effects of laser power and feed speed on absorptivity in the proposed thermal model, an empirical formula of absorptivity is obtained by least squares fitting:

$$a_0 = c_1 {P_0}^{c_2} F^{c_3} \tag{7}$$

where c_1, c_2, and c_3 are three constant coefficients, and the fitted results are equal to 0.5652, −0.1536, and 0.0793, respectively.

The above absorptivity formula was used in the thermal model to predict the peak temperature under each experimental condition; then, the predicted result was compared with the measured one. As displayed in Table 3, the maximum relative error is about 3.3%.

Table 4 Laser heating experimental parameters (verification experiments)

No.	Power (W)	Feed speed (mm/min)
10	200	100
11	400	100
12	600	100
13	800	100
14	1000	100
15	1000	250
16	1000	200
17	1000	150
18	1000	50

Table 5 Prediction results of HAZ

No.	HAZ width (mm)	HAZ depth (mm)
10	0	0
11	1.3	0.1
12	3.1	0.75
13	3.5	1.3
14	3.85	1.8
15	3.25	0.9
16	3.4	1.1
17	3.6	1.4
18	4.25	2.4

4 Model verification and discussion

Laser heating and LAM experiments were carried out in this workpiece. XRD technique was employed to analyze the microstructures in the heated and machined surface layers. Based on the qualitative and quantitative analyses of phase composition, the HAZ model presented in this paper was verified. Besides, the influences of different laser parameters on the HAZ were theoretically investigated.

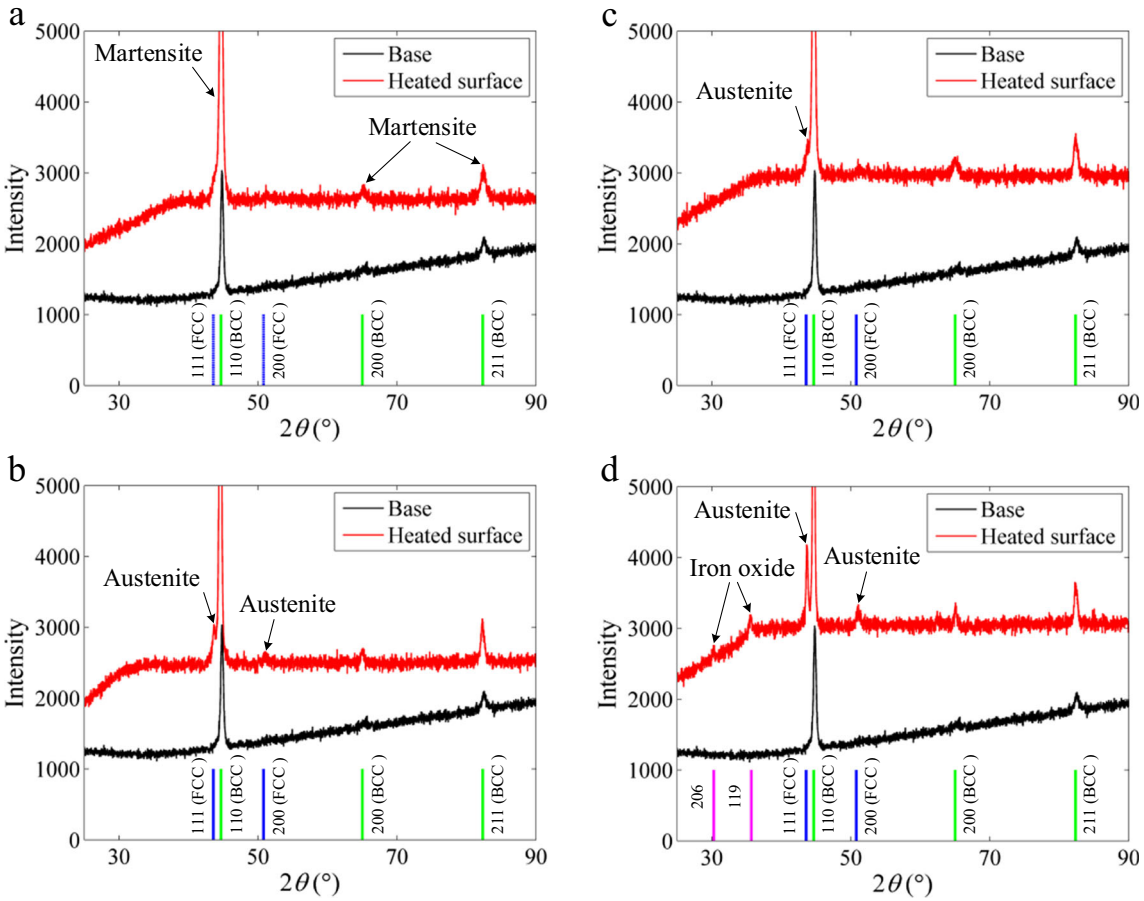

Fig. 6 Diffractograms taken on specimens: **a** No. 10, **b** No. 14, **c** No. 15, **d** No. 18

4.1 Laser heating experiments

As shown in Table 4, a series of laser heating experiments were designed to validate the HAZ model. Other laser parameters are the same with those in Section 3.1. The size of the HAZ under each experimental condition is calculated, and the results are listed in Table 5. According to the prediction results, no phase transformation occurs in experiment no. 10. In addition, the size of the HAZ increases with increasing laser power and decreases with increasing feed speed.

After laser heating experiments, XRD specimens were cut from the workpiece by WEDM. Then, the phase compositions in the heated surface of each specimen were detected using an X-ray diffraction instrument (PANalytical B.V., X'Pert^3 Powder). The X-ray tube was Cu_K-Alpha; the voltage and current were set to 40 kV and 40 mA respectively. The scan

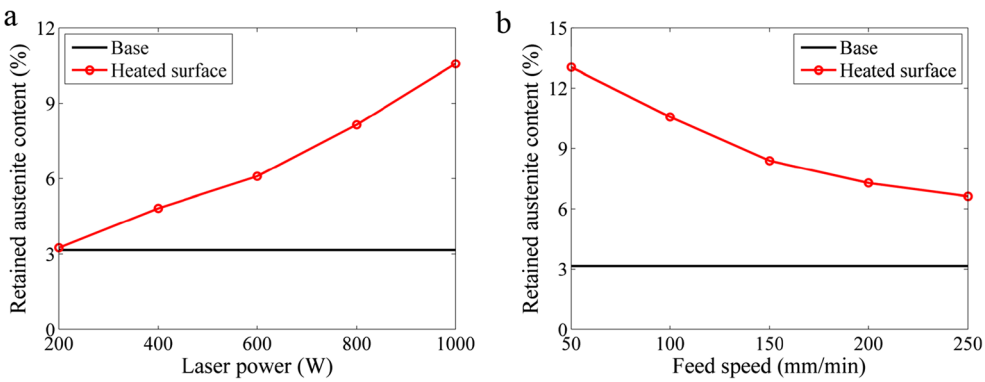

Fig. 7 Influences of different laser parameters on retained austenite content: **a** laser power (Nos. 10–14), **b** feed speed (Nos. 14–18)

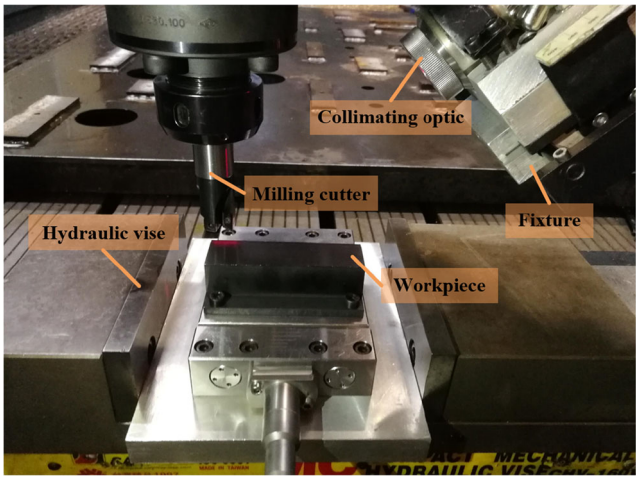

Fig. 8 LAM experimental image

range was 10–90°; the scan speed was 8°/min. After X-ray scanning of the heated surfaces, the obtained ".rd" files were imported into the data processing software MDI Jade 6; then PDF99-0064, PDF33-0397, and PDF25-1402 cards were employed to accomplish the detection of phase compositions.

Phase compositions of each specimen were compared with those of the base material. The X-ray diffractograms from partial specimens are shown in Fig. 6. Face center cubic (FCC) and body center cubic (BCC) refer to austenite and martensite, respectively. The results show that almost no austenite was detected in the base material. And an obvious austenite transformation occurred in all experiments except experiment no. 10. This is consistent with the prediction results shown in Table 5. Besides, the height of the 111 peak represents a positive correlation between the content of austenite and the laser power, and a negative correlation between the content of austenite and the feed speed. This is identical with the variation trend of HAZ (Table 5).

As displayed in Fig. 6d, iron oxide (206 and 119 peaks) was detected in specimen no. 18. According to the thermal model proposed in Section 2.1, the heating temperature under the condition of experiment no. 18 is the highest, and exceeds the melting point of AerMet100 steel. Therefore, this experimental phenomenon is mainly caused by the oxidation of workpiece material during laser heating.

In order to obtain the retained austenite content quantitatively, the specimens were tested using an X-ray analysis system (PROTO iXRD). The X-ray tube was Cr_K-Alpha, and a filter made of vanadium was installed on the tube. The collimator was 2 mm in diameter. The voltage and current were set to 20 kV and 4 mA, respectively. The Bragg angle is 156.41°. The X-rays made multiple exposures to the measured area, and four diffraction peaks were collected, two for the ferrite/martensite phase and two for the austenite phase. Combined with the software XRDWIN, the volume percent concentration of retained austenite in the sample was obtained by comparing the intensities of the 4 peaks' yields. The result shows the retained austenite content in the base material was about 3.16%. This is why the austenite peaks are hardly visible in the XRD pattern of base material (Fig. 6).

As shown in Fig. 7, the retained austenite content of specimen no. 10 is almost unchanged compared with that of the base material. In addition, the retained austenite content increases with increasing laser power and decreases with increasing feed speed. This is consistent with the above qualitative analysis results.

Considering that the change in retained austenite content reflects the degree of austenization and the size of the HAZ, the experimental phenomena observed in this section indirectly validate the HAZ model presented in this paper.

4.2 LAM experiments

In order to demonstrate the validity of the HAZ model in determining the process parameters that yields no residual HAZ in the machined surface layer, several LAM experiments were conducted in this section. As can be seen in Fig. 8, a square shoulder milling cutter (Kennametal, STELLRAM 7690VA12CA025Z03R40-3) with 25-mm diameter was used in this study. And a new carbide insert (Kennametal, ADHT12T308ER-46 SP6519) was used in each experiment.

The experimental scheme is shown in Table 6. Radial depth of cut, axial depth of cut, and laser-tool distance are kept invariant, and equal to 4 mm, 2 mm, and 13 mm respectively. Other laser parameters are the same with those in Section 3.1.

The width and depth of the HAZ under different experimental conditions are predicted and compared with the cutting depth, as shown in Fig. 9. It can be found that the HAZ width in experiment no. 20 is larger than the radial depth of cut, and the HAZ depth is larger than the axial depth of cut. Theoretically, there will be residual HAZ in the machined surface layer of experiment no. 20. Besides, the HAZ width in experiment no. 22 is smaller than the radial depth of cut, and the HAZ depth is smaller than the axial depth of cut. Therefore, the HAZ produced in experiment mo. 22 will be completely removed.

Table 6 LAM experimental parameters

No.	Spindle speed (r/min)	Feed speed (mm/min)	Radial depth of cut (mm)	Axial depth of cut (mm)	Laser power (W)
19	1000	50	4	2	0
20	1000	50	4	2	1000
21	2000	300	4	2	0
22	2000	300	4	2	1000

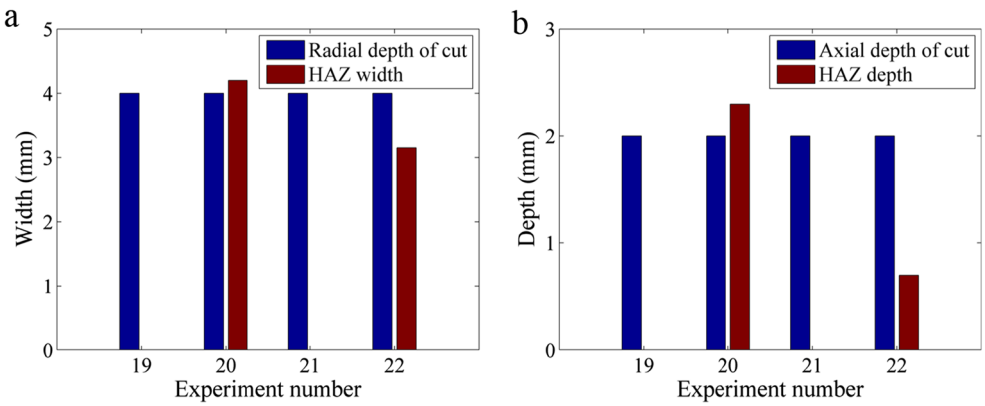

Fig. 9 Comparison of HAZ size and cutting depth: **a** comparison of HAZ width and radial depth of cut, **b** comparison of HAZ depth and axial depth of cut

After machining experiments, XRD tests were conducted to detect the retained austenite content in each machined surface. The measured results were compared with the retained austenite content in the base material, as can be seen in Fig. 10. It can be found that conventional milling process (experiments no. 19 and 21) has little effect on the retained austenite content. In particular, the retained austenite content in the machined surface of experiment no. 20 is much higher than that of the base material, which confirms the existence of residual HAZ in the workpiece after machining. Besides, the retained austenite content in the machined surface of experiment no. 22 is close to that of the base material, which indicates that the HAZ is indeed completely removed. The consistence between experimental and predicted results demonstrates the utility of the proposed HAZ model.

4.3 Influences of laser parameters on HAZ

In this section, the impacts of different laser parameters on the width and depth of the HAZ are theoretically investigated.

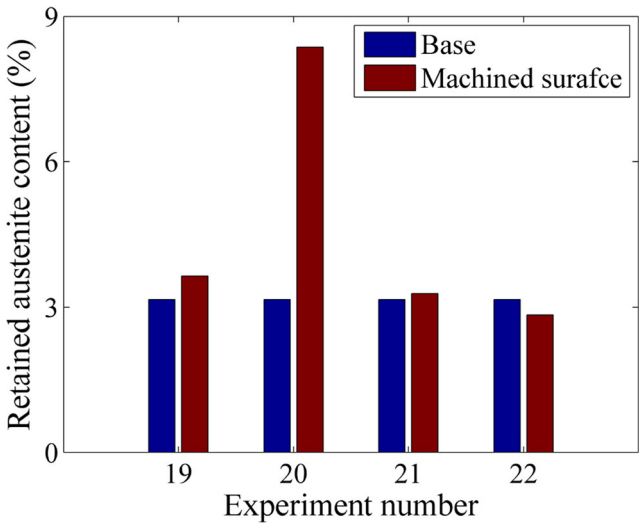

Fig. 10 Comparison of retained austenite content between machined surface and base material

The results show that the size of the HAZ increases significantly with increasing laser power (Fig. 11), and decreases significantly with increasing feed speed (Fig. 12). The reason is that both laser power and feed speed have a strong influence on the workpiece temperature. As shown in Fig. 13, there is a critical laser power for the occurrence of HAZ. This is because the maximum temperature in workpiece is lower than T_0 when the laser power is less than the critical value.

Figure 13 shows that the laser spot size (semi-minor axis) has an opposite effect on the width and depth of the HAZ. It is not hard to understand that the smaller the laser spot size, the more concentrated the energy, and vice versa. Therefore, the HAZ width increases with the increase of laser spot size, and it appears the opposite change for the HAZ depth. For this reason, a small laser spot is recommended for side milling, and a large laser spot is recommended for face milling. Compared with other laser parameters, the laser incident angle has little impact on HAZ. As shown in Fig. 13, the size of the HAZ decreases slightly with increasing laser incident angle.

To ensure the machined surface quality in LAM, the HAZ depth should be controlled less than the axial depth of cut. In addition, for the side milling studied in this paper, the HAZ width should be controlled less than the radial depth of cut. Under any given cut geometry and feed speed, the size of the HAZ can be effectively controlled by adjusting the laser power and spot size.

5 Conclusions

In this paper, an analytical model is established to predict the HAZ produced by laser heating in LAM process. According to the experimental and predicted results, as well as the analyses reported above, the following conclusions can be drawn:

1. XRD analysis results are consistent with the predicted results of HAZ. This indicates that the presented model is feasible.
2. The size of the HAZ increases significantly with increasing laser power and decreases significantly with

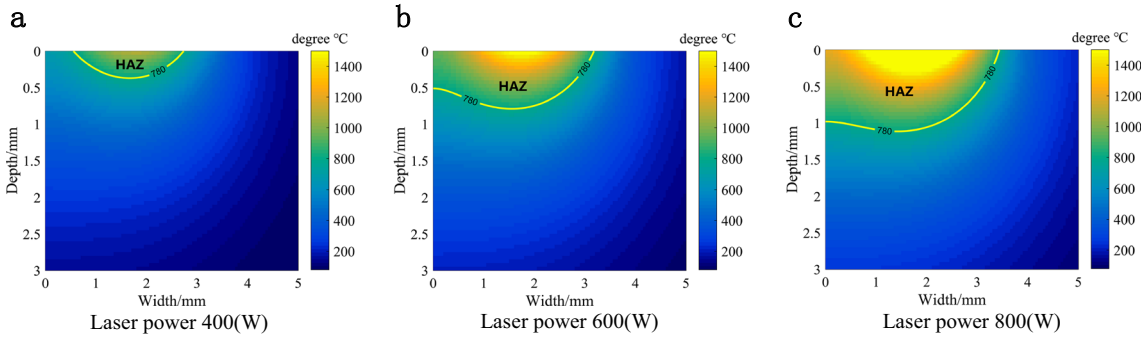

Fig. 11 The size of HAZ affected by different laser powers with the same feed speed 300 mm/min: **a** 400 W, **b** 600 W, **c** 800 W

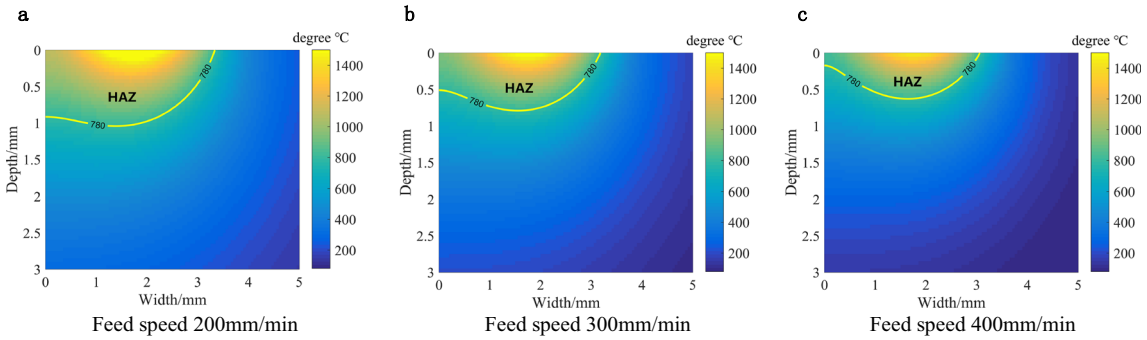

Fig. 12 The size of HAZ affected by different feed speeds with the same laser power 600 W: **a** 200 mm/min, **b** 300 mm/min, **c** 400 mm/min

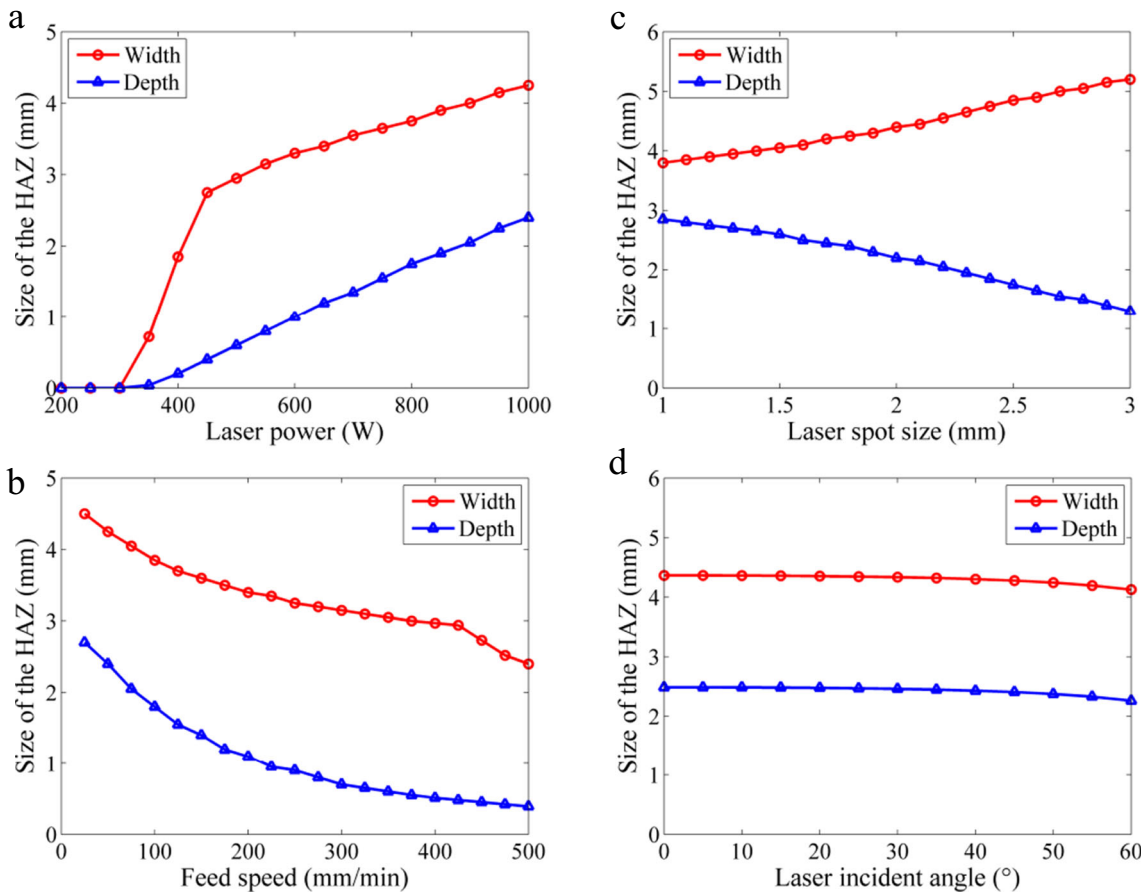

Fig. 13 Influences of different laser parameters on HAZ: **a** laser power, **b** feed speed, **c** laser spot size, **d** laser incident angle

increasing feed speed. The HAZ width increases with the increase of laser spot size, and it appears the opposite change for the HAZ depth. In view of this, a small laser spot is recommended for side milling, and a large laser spot is recommended for face milling.

3. This work can be applied in future studies to determine the process parameters in LAM that will yield no residual HAZ in the workpiece after machining.

Funding information This work was financially supported by the National Natural Science Foundation of China (51775213, 91860206) and the National Science Foundation for Distinguished Young Scholars of China (51625502).

References

1. Yao C, Wang T, Xiao W, Huang X, Ren J (2014) Experimental study on grinding force and grinding temperature of Aermet 100 steel in surface grinding. J Mater Process Technol 214(11):2191–2199
2. Zeng H, Yan R, Du P, Zhang M, Peng F (2018) Notch wear prediction model in high speed milling of AerMet100 steel with bull-nose tool considering the influence of stress concentration. Wear 408-409:228–237
3. Hedberg GK, Shin YC, Xu L (2015) Laser-assisted milling of Ti-6Al-4V with the consideration of surface integrity. Int J Adv Manuf Technol 79:1645–1658
4. Kashani MM, Movahhedy MR, Ahmadian MT (2017) In-process determination of laser beam absorption coefficient for laser-assisted turning processes. Int J Adv Manuf Technol 92:2929–2938
5. Wiedenmann R, Zaeh MF (2015) Laser-assisted milling—process modeling and experimental validation. CIRP J Manuf Sci Technol 8:70–77
6. Sun S, Brandt M, Barnes JE, Dargusch MS (2011) Experimental investigation of cutting forces and tool wear during laser-assisted milling of Ti-6Al-4V alloy. Proc Inst Mech Eng B J Eng Manuf 225(9):1512–1527
7. Bermingham MJ, Kent D, Dargusch MS (2015) A new understanding of the wear processes during laser assisted milling 17-4 precipitation hardened stainless steel. Wear 328:518–530
8. Wiedenmann R, Langhorst M, Zaeh MF (2011) Computerized optimization of the process parameters in laser-assisted milling. Phys Procedia 12:607–616
9. Tagliaferri F, Leopardi G, Semmler U, Kuhl M, Palumbo B (2013) Study of the influences of laser parameters on laser assisted machining processes. Procedia CIRP 8:170–175
10. Pan Z, Feng Y, Hung TP, Jiang YC, Hsu FC, Wu LT, Lin CF, Lu YC, Liang SY (2017) Heat affected zone in the laser-assisted milling of Inconel 718. J Manuf Process 30:141–147
11. Singh R, Alberts MJ, Melkote SN (2008) Characterization and prediction of the heat-affected zone in a laser-assisted mechanical micromachining process. Int J Mach Tools Manuf 48(9):994–1004
12. Yang J, Sun S, Brandt M, Yan W (2010) Experimental investigation and 3D finite element prediction of the heat affected zone during laser assisted machining of Ti6Al4V alloy. J Mater Process Technol 210(15):2215–2222
13. Rahim EA, Warap NM, Mohid Z, Ibrahim R, Rafai N (2015) Numerical analysis of laser preheating for laser assisted micro milling of Inconel 718. Appl Mech Mater 773-774:332–336
14. Hedberg GK, Shin YC (2015) Laser assisted milling of Ti-6Al-4V ELI with the analysis of surface integrity and its economics. Lasers Manuf Mater Process 2(3):164–185
15. Woo WS, Lee CM (2015) A study of the machining characteristics of AISI 1045 steel and Inconel 718 with a cylindrical shape in laser-assisted milling. Appl Therm Eng 91:33–42
16. Shang Z, Liao Z, Sarasua JA, Billingham J, Axinte D (2019) On modelling of laser assisted machining: forward and inverse problems for heat placement control. Int J Mach Tools Manuf 138:36–50
17. Zaeh MF, Wiedenmann R, Daub R (2010) A thermal simulation model for laser-assisted milling. Phys Procedia 5:353–362
18. Kim DH, Lee CM (2014) A study of cutting force and preheating-temperature prediction for laser-assisted milling of Inconel 718 and AISI 1045 steel. Int J Heat Mass Transfer 71(4):264–274
19. Carslaw HS, Jaeger JC (1959) Conduction of heat in solids. Clarendon Press, Oxford
20. Kumar M, Chang CJ, Melkote SN, Joseph VR (2013) Modeling and analysis of forces in laser assisted micro milling. Trans ASME J Manuf Sci Eng 135(4):041018
21. Lin S, Peng F, Wen J, Liu Y, Yan R (2013) An investigation of workpiece temperature variation in end milling considering flank rubbing effect. Int J Mach Tools Manuf 73(7):71–86
22. Feng Y, Hung TP, Lu YT, Lin YF, Hsu FC, Lin CF, Lu YC, Liang SY (2019) Analytical prediction of temperature in laser-assisted milling with laser preheating and machining effects. Int J Adv Manuf Technol 100:3185–3195
23. Mirkoohi E, Bocchini P, Liang SY (2019) Analytical temperature predictive modeling and non-linear optimization in machining. Int J Adv Manuf Technol 102(5–8):1557–1566
24. Zeng H, Yan R, Hu T, Du P, Wang W, Peng F (2019) Analytical modeling of white layer formation in orthogonal cutting of AerMet100 steel based on phase transformation mechanism. Trans ASME J Manuf Sci Eng 141(6):064502